

Shock-capturing non-hydrostatic model for fully dispersive surface wave processes

Gangfeng Ma*, Fengyan Shi, James T. Kirby

Center for Applied Coastal Research, University of Delaware, Newark, DE 19716, USA

ARTICLE INFO

Article history:

Received 16 June 2011

Received in revised form 30 November 2011

Accepted 4 December 2011

Available online 21 December 2011

Keywords:

Non-hydrostatic model

Shock-capturing

Godunov-type scheme

Nearshore wave processes

Landslide generated tsunami

Longshore current

ABSTRACT

This paper describes NHWAVE, a shock-capturing non-hydrostatic model for simulating wave refraction, diffraction, shoaling, breaking and landslide-generated tsunami in finite water depth. The governing equations are the incompressible Navier–Stokes equations in conservative form, written in surface and terrain-following form using a σ coordinate. In order to apply a Godunov-type scheme, the velocities are defined at cell centers. The dynamic pressure is defined at vertically facing cell faces so that the pressure boundary condition at free surface can be precisely imposed. The HLL Riemann approximation is employed to estimate fluxes at horizontal cell faces. The nonlinear Strong Stability-Preserving (SSP) Runge–Kutta scheme is used to obtain second-order accuracy in time. The model is validated using seven test cases based on analytical solutions and experimental data. The computed results show that the model can well predict wave propagation over submerged bar, wave refraction and diffraction over an elliptical shoal as well as wave breaking, run-up and longshore current on a plane beach using relatively few (three to five) vertical layers. The model is also shown to provide accurate reproduction of a generated tsunami wave resulting from a solid translating bottom feature.

Published by Elsevier Ltd.

1. Introduction

Wave propagation from deep water to coastal region is subject to wave refraction, diffraction, shoaling and breaking. Accurate prediction of these phenomena is crucial to studying nearshore hydrodynamics and solute transport in the coastal area. Boussinesq-type wave models with improved nonlinearity and dispersion characteristics provide an efficient and well-tested tool for the simulation of wave propagation, especially in shallow water regions (Madsen and Sørensen, 1992; Nwogu, 1993; Wei et al., 1995). Means for extending these models to higher order in dispersion have been developed (see Gobbi et al. (2000), Lynett and Liu (2002) and Agnon et al. (1999), for example), and more recently, extensions to the model formulation to account for turbulent structure of the flow field and the resulting effects on depth-averaged solute or contaminant transport have been developed (Kim et al., 2009; Kim and Lynett, 2011). All of these extensions lead to a great deal of complexity in the resulting model equations.

An alternative approach is to solve the Navier–Stokes equations directly with proper free surface tracking techniques, such as the marker-and-cell (MAC) method (Harlow and Welch, 1965), the volume-of-fluid (VOF) method (Hirt and Nichols, 1981) and the level-set method (Osher and Sethian, 1988). These approaches

have wide applications on the simulations of wave shoaling and breaking in the surf zone; see, for example, Lin and Liu (1998a,b), Watanabe et al. (2005), Christensen (2006), Shi et al. (2010) and Ma et al. (2011). The main drawbacks of these types of models are: (1) they are computationally expensive, making applications to large-scale domains infeasible; (2) the free surface normally crosses the computational cell arbitrarily, which brings the difficulty of applying the pressure boundary condition precisely on the free surface and may eventually affect the accuracy of velocity computation (Lin and Li, 2002); and (3) the grid resolution in the surf zone and swash zone, where the water depth is relatively shallow, is usually poor due to the use of Cartesian grid system on most of applications.

A direct simplification of the above-mentioned approach is to assume that the free surface elevation is a single value function of the horizontal coordinates. By doing so, the free surface is always located at the upper computational boundary and can be determined by applying the free surface boundary conditions. It is computationally more efficient with the lack of free surface tracking. The pressure boundary condition at the free surface can be accurately prescribed with some proper treatments. This simplification leads to a new set of non-hydrostatic models, which are not only suitable for modeling short wave propagation but also for the simulation of turbulence and solute transport in the surf zone. To solve the non-hydrostatic equations, the pressure is decomposed into hydrostatic and non-hydrostatic components. The governing equations can be discretized by finite difference

* Corresponding author. Tel.: +1 302 256 3163; fax: +1 302 831 1228.

E-mail address: gma@udel.edu (G. Ma).

method (Casulli and Stelling, 1998; Casulli, 1999; Namin et al., 2001; Casulli and Zanolli, 2002; Lin and Li, 2002; Chen, 2003; Stelling and Zijlema, 2003; Zijlema and Stelling, 2005; Yuan and Wu, 2004a,b; Lee et al., 2006; Young et al., 2007, 2009; Young and Wu, 2010; Wu et al., 2010), finite element method (Walters, 2005) and finite volume method (Bradford, 2005; Fringer et al., 2006; Ai and Jin, 2010; Lai et al., 2010). A major concern addressed in recent developments of non-hydrostatic models is the accurate prediction of wave dispersion characteristics with relatively few vertical grid points. It has been recognized that 10–20 vertical layers are normally required to describe wave dispersion up to an acceptable level with some simple treatments of pressure boundary conditions at the top layer, for example, Casulli and Stelling (1998), Casulli (1999), Casulli and Zanolli (2002), Li and Fleming (2001), Namin et al. (2001), Lin and Li (2002) and Chen (2003). To address this issue, Stelling and Zijlema (2003) proposed the Keller-box method to replace the staggered grid in the vertical direction, which enables the pressure to be located at the cell faces rather than the cell centers. The pressure boundary condition at the free surface can be exactly assigned to zero without any approximation. Yuan and Wu (2004a,b) proposed an integral method to remove the top-layer hydrostatic assumption using a staggered grid framework. Young and Wu (2010) used the Boussinesq-type-like equations with the reference velocity to provide an analytical-based non-hydrostatic pressure distribution at the top layer. All of these methods significantly reduce the errors in dynamic pressure estimation and allow for use of a very small number of vertical layers for accurate simulation of dispersive waves.

It is non-trivial to apply non-hydrostatic models to the simulation of breaking waves in the surf zone and wave run-up in the swash region, because the numerical scheme involved must treat shock propagation adequately in order to model broken waves (Zijlema and Stelling, 2008). Shock-capturing schemes based on Godunov-type approach, which can deal with discontinuous flow, are well-suited for breaking wave simulations. These schemes are able to track actual location of wave breaking without requiring any criterion that tells the model when and where the wave breaking happens. An application of this approach to simulation of breaking waves in the surf zone was given by Bradford (2011). It was showed that the non-hydrostatic model with Godunov-type scheme can predict wave height distribution, turbulence and undertow under breaking waves at least as accurate as the VOF model. However, eight or more vertical layers are needed in his model to accurately predict the surface elevation around the outer surf zone as well as velocity profiles within the surf zone.

In this paper, we describe a new nonhydrostatic model (called NHWAVE, for Non Hydrostatic WAVE model) based on a Godunov-type scheme. NHWAVE solves the incompressible Navier–Stokes equations in terrain and surface-following σ coordinates. Bottom movement is included in order to simulate tsunami generation by three-dimensional underwater landslides. To apply Godunov-type scheme, the velocities are defined at cell centers. The dynamic pressure is defined at vertically-facing cell faces as in the Keller-box method, allowing the pressure boundary condition at the free surface to be precisely imposed. The hydrostatic equations are solved by a well-balanced finite volume method. The fluxes at cell faces are estimated by HLL Riemann approximation. To obtain second-order temporal accuracy, the nonlinear Strong Stability-Preserving (SSP) Runge–Kutta scheme (Gottlieb et al., 2001) is adopted for adaptive time stepping. The model is fully parallelized using Message Passing Interface (MPI) with non-blocking communication. The poisson equation is solved by the high performance preconditioner HYPRE software library (<http://acts.nersc.gov/hypre/>).

The paper is organized as follows. In Section 2, the governing equations in conservative form are presented. The numerical method, boundary conditions and wetting–drying scheme are introduced

in Section 3. Finally, seven test cases are given in Section 4 to show the model's capability of simulating wave refraction, diffraction, shoaling, breaking, landslide tsunami generation and longshore current.

2. Governing equations

The incompressible Navier–Stokes equations in Cartesian coordinates (x_1^*, x_2^*, x_3^*) , where $x_1^* = x^*$, $x_2^* = y^*$ and $x_3^* = z^*$ and time t^* are given by

$$\frac{\partial u_i}{\partial x_i^*} = 0 \quad (1)$$

$$\frac{\partial u_i}{\partial t^*} + u_j \frac{\partial u_i}{\partial x_j^*} = -\frac{1}{\rho} \frac{\partial p}{\partial x_i^*} + g_i + \frac{\partial \tau_{ij}}{\partial x_j^*} \quad (2)$$

where $(i, j) = 1, 2, 3$, u_i is velocity component in the x_i^* direction, p is total pressure, ρ is water density, $g_i = -g\delta_{i3}$ is the gravitational body force and $\tau_{ij} = \nu_t (\partial u_i / \partial x_j^* + \partial u_j / \partial x_i^*)$ is turbulent stress with ν_t the turbulent kinematic viscosity.

In order to accurately represent bottom and surface geometry, a σ -coordinate developed by Phillips (1957) is adopted in this study

$$t = t^* \quad x = x^* \quad y = y^* \quad \sigma = \frac{z^* + h}{D} \quad (3)$$

where $D(x, y, t) = h(x, y, t) + \eta(x, y, t)$, h is water depth, η is surface elevation. This coordinate transformation basically maps the varying vertical coordinate in the physical domain to a uniform transformed space where σ spans from 0 to 1 (Lin and Li, 2002). Using the principle of chain differentiation, the partial differentiation of a variable $f = f(x^*, y^*, z^*, t^*)$ in the physical domain is transformed as follows:

$$\begin{aligned} \frac{\partial f}{\partial t^*} &= \frac{\partial f}{\partial t} + \frac{\partial f}{\partial \sigma} \frac{\partial \sigma}{\partial t^*} \\ \frac{\partial f}{\partial x^*} &= \frac{\partial f}{\partial x} + \frac{\partial f}{\partial \sigma} \frac{\partial \sigma}{\partial x^*} \\ \frac{\partial f}{\partial y^*} &= \frac{\partial f}{\partial y} + \frac{\partial f}{\partial \sigma} \frac{\partial \sigma}{\partial y^*} \\ \frac{\partial f}{\partial z^*} &= \frac{\partial f}{\partial \sigma} \frac{\partial \sigma}{\partial z^*} \end{aligned} \quad (4)$$

Plugging Eq. (4) into (1) and (2), we obtain the governing equations in the new coordinate (x, y, σ) and time t

$$\frac{\partial D}{\partial t} + \frac{\partial Du}{\partial x} + \frac{\partial Dv}{\partial y} + \frac{\partial \omega}{\partial \sigma} = 0 \quad (5)$$

$$\frac{\partial \mathbf{U}}{\partial t} + \frac{\partial \mathbf{F}}{\partial x} + \frac{\partial \mathbf{G}}{\partial y} + \frac{\partial \mathbf{H}}{\partial \sigma} = \mathbf{S}_h + \mathbf{S}_p + \mathbf{S}_\tau \quad (6)$$

where $\mathbf{U} = (Du, Dv, D\omega)^T$. The fluxes are

$$\mathbf{F} = \begin{pmatrix} Duu + \frac{1}{2}gD^2 \\ Du v \\ Du w \end{pmatrix} \quad \mathbf{G} = \begin{pmatrix} Duv \\ Dvv + \frac{1}{2}gD^2 \\ Dvw \end{pmatrix} \quad \mathbf{H} = \begin{pmatrix} u\omega \\ v\omega \\ w\omega \end{pmatrix}$$

The source terms are given by

$$\mathbf{S}_h = \begin{pmatrix} gD \frac{\partial h}{\partial x} \\ gD \frac{\partial h}{\partial y} \\ 0 \end{pmatrix} \quad \mathbf{S}_p = \begin{pmatrix} -\frac{D}{\rho} \left(\frac{\partial p}{\partial x} + \frac{\partial p}{\partial \sigma} \frac{\partial \sigma}{\partial x^*} \right) \\ -\frac{D}{\rho} \left(\frac{\partial p}{\partial y} + \frac{\partial p}{\partial \sigma} \frac{\partial \sigma}{\partial y^*} \right) \\ -\frac{1}{\rho} \frac{\partial p}{\partial \sigma} \end{pmatrix} \quad \mathbf{S}_\tau = \begin{pmatrix} DS_{\tau_x} \\ DS_{\tau_y} \\ DS_{\tau_z} \end{pmatrix}$$

where the total pressure has been divided into two parts: dynamic pressure p (use p as dynamic pressure hereinafter for simplicity) and hydrostatic pressure $\rho g(\eta - z)$. ω is the vertical velocity in the σ coordinate image domain, given by

$$\omega = D \left(\frac{\partial \sigma}{\partial t^*} + u \frac{\partial \sigma}{\partial x^*} + v \frac{\partial \sigma}{\partial y^*} + w \frac{\partial \sigma}{\partial z^*} \right) \quad (7)$$

with

$$\begin{aligned}\frac{\partial \sigma}{\partial t^*} &= \frac{1}{D} \frac{\partial h}{\partial t} - \frac{\sigma}{D} \frac{\partial D}{\partial t} \\ \frac{\partial \sigma}{\partial x^*} &= \frac{1}{D} \frac{\partial h}{\partial x} - \frac{\sigma}{D} \frac{\partial D}{\partial x} \\ \frac{\partial \sigma}{\partial y^*} &= \frac{1}{D} \frac{\partial h}{\partial y} - \frac{\sigma}{D} \frac{\partial D}{\partial y} \\ \frac{\partial \sigma}{\partial z^*} &= \frac{1}{D}\end{aligned}\quad (8)$$

In the current paper, turbulent diffusion terms S_{τ_x} , S_{τ_y} , S_{τ_z} are included for the cases involving wave breaking, which are given by

$$\begin{aligned}S_{\tau_x} &= \frac{\partial \tau_{xx}}{\partial x} + \frac{\partial \tau_{xx}}{\partial \sigma} \frac{\partial \sigma}{\partial x^*} + \frac{\partial \tau_{xy}}{\partial y} + \frac{\partial \tau_{xy}}{\partial \sigma} \frac{\partial \sigma}{\partial y^*} + \frac{\partial \tau_{xz}}{\partial z} + \frac{\partial \tau_{xz}}{\partial \sigma} \frac{\partial \sigma}{\partial z^*} \\ S_{\tau_y} &= \frac{\partial \tau_{yx}}{\partial x} + \frac{\partial \tau_{yx}}{\partial \sigma} \frac{\partial \sigma}{\partial x^*} + \frac{\partial \tau_{yy}}{\partial y} + \frac{\partial \tau_{yy}}{\partial \sigma} \frac{\partial \sigma}{\partial y^*} + \frac{\partial \tau_{yz}}{\partial z} + \frac{\partial \tau_{yz}}{\partial \sigma} \frac{\partial \sigma}{\partial z^*} \\ S_{\tau_z} &= \frac{\partial \tau_{zx}}{\partial x} + \frac{\partial \tau_{zx}}{\partial \sigma} \frac{\partial \sigma}{\partial x^*} + \frac{\partial \tau_{zy}}{\partial y} + \frac{\partial \tau_{zy}}{\partial \sigma} \frac{\partial \sigma}{\partial y^*} + \frac{\partial \tau_{zz}}{\partial z} + \frac{\partial \tau_{zz}}{\partial \sigma} \frac{\partial \sigma}{\partial z^*}\end{aligned}\quad (9)$$

and the stresses in the transformed space are calculated as

$$\begin{aligned}\tau_{xx} &= 2\nu_t \left(\frac{\partial u}{\partial x} + \frac{\partial u}{\partial \sigma} \frac{\partial \sigma}{\partial x^*} \right) & \tau_{xy} &= \tau_{yx} = \nu_t \left(\frac{\partial u}{\partial y} + \frac{\partial u}{\partial \sigma} \frac{\partial \sigma}{\partial y^*} + \frac{\partial v}{\partial x} + \frac{\partial v}{\partial \sigma} \frac{\partial \sigma}{\partial x^*} \right) \\ \tau_{yy} &= 2\nu_t \left(\frac{\partial v}{\partial y} + \frac{\partial v}{\partial \sigma} \frac{\partial \sigma}{\partial y^*} \right) & \tau_{xz} &= \tau_{zx} = \nu_t \left(\frac{\partial u}{\partial z} + \frac{\partial w}{\partial x} + \frac{\partial w}{\partial \sigma} \frac{\partial \sigma}{\partial x^*} \right) \\ \tau_{zz} &= 2\nu_t \left(\frac{\partial w}{\partial z} + \frac{\partial w}{\partial \sigma} \frac{\partial \sigma}{\partial z^*} \right) & \tau_{yz} &= \tau_{zy} = \nu_t \left(\frac{\partial v}{\partial z} + \frac{\partial w}{\partial y} + \frac{\partial w}{\partial \sigma} \frac{\partial \sigma}{\partial y^*} \right)\end{aligned}\quad (10)$$

The turbulent kinematic viscosity ν_t is estimated by the Smagorinsky subgrid model

$$\nu_t = (C_s \Delta)^2 \sqrt{2S_{ij}S_{ij}} \quad (11)$$

where C_s is the Smagorinsky coefficient, which is taken as 0.1–0.2, Δ is the filter width, which is calculated as $\Delta = (\Delta x \Delta y \Delta \sigma D)^{1/3}$, and $S_{ij} = \frac{1}{2} \left(\frac{\partial u_i}{\partial x_j} + \frac{\partial u_j}{\partial x_i} \right)$ is the stress tensor.

Integrating Eq. (5) from $\sigma = 0$ to 1 and using the boundary conditions at the bottom and surface for ω , we get the governing equation for free surface movement.

$$\frac{\partial D}{\partial t} + \frac{\partial}{\partial x} \left(D \int_0^1 u d\sigma \right) + \frac{\partial}{\partial y} \left(D \int_0^1 v d\sigma \right) = 0 \quad (12)$$

3. Numerical method

A combined finite-volume and finite-difference scheme with a Godunov-type method was applied to discretize equations (6) and (12). It is straightforward to define all dependent variables at cell centers to solve Riemann problem. However, this treatment results in checkerboard solutions in which the pressure and velocity become decoupled when they are defined at the same location (Patankar, 1980). Therefore, most existing models use a staggered grid in which the pressure is defined at the centers of computational cells and the velocities are defined at cell faces (Bradford, 2005). However, staggered grids do not lend themselves as easily as co-located grids to the use of Godunov-type schemes. Meanwhile, difficulty in treating the cell-centered pressure at the top layer may arise when applying the pressure boundary condition at the free surface (Yuan and Wu, 2004a,b).

With these considerations, a different kind of staggered grid framework is introduced, in which the velocities are placed at the cell centers and the pressure is defined at the vertically-facing cell faces as shown in Fig. 1. The momentum equations are solved

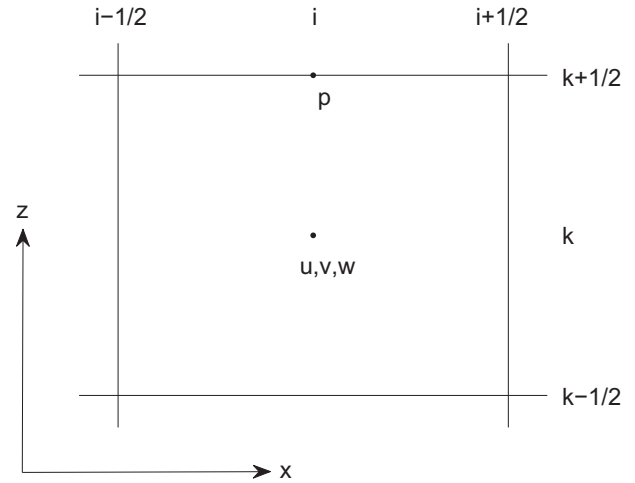


Fig. 1. Layout of computational variables. Velocities (u, v, w) are placed at cell center and dynamic pressure (p) is defined at vertical cell face.

by a second-order Godunov-type finite volume method. The HLL approximate Riemann solver (Harten et al., 1983) is used to estimate fluxes at the cell faces. As in Stelling and Zijlema (2003), the pressure boundary condition at the free surface can be precisely assigned to zero.

3.1. Time stepping

To obtain second-order temporal accuracy, the two-stage second-order nonlinear Strong Stability-Preserving (SSP) Runge–Kutta scheme (Gottlieb et al., 2001) was adopted for time stepping. At the first stage, an intermediate quantity $\mathbf{U}^{(1)}$ is evaluated using a typical first-order, two-step projection method given by

$$\frac{\mathbf{U}^* - \mathbf{U}^n}{\Delta t} = - \left(\frac{\partial \mathbf{F}}{\partial x} + \frac{\partial \mathbf{G}}{\partial y} + \frac{\partial \mathbf{H}}{\partial \sigma} \right)^n + \mathbf{S}_h^n + \mathbf{S}_\tau^n \quad (13)$$

$$\frac{\mathbf{U}^{(1)} - \mathbf{U}^*}{\Delta t} = \mathbf{S}_p^{(1)} \quad (14)$$

where \mathbf{U}^n represents \mathbf{U} value at time level n , \mathbf{U}^* is the intermediate value in the two-step projection method, and $\mathbf{U}^{(1)}$ is the final first stage estimate. In the second stage, the velocity field is again updated to a second intermediate level using the same projection method, after which the Runge–Kutta algorithm is used to obtain a final value of the solution at the $n + 1$ time level

$$\frac{\mathbf{U}^* - \mathbf{U}^{(1)}}{\Delta t} = - \left(\frac{\partial \mathbf{F}}{\partial x} + \frac{\partial \mathbf{G}}{\partial y} + \frac{\partial \mathbf{H}}{\partial \sigma} \right)^{(1)} + \mathbf{S}_h^{(1)} + \mathbf{S}_\tau^{(1)} \quad (15)$$

$$\frac{\mathbf{U}^{(2)} - \mathbf{U}^*}{\Delta t} = \mathbf{S}_p^{(2)} \quad (16)$$

$$\mathbf{U}^{n+1} = \frac{1}{2} \mathbf{U}^n + \frac{1}{2} \mathbf{U}^{(2)} \quad (17)$$

Each stage of the calculation requires the specification of the non-hydrostatic component of the pressure force as expressed through the quantities \mathbf{S}_p . The pressure field needed to specify these is based on the solution of the Poisson equation described below. Also at each stage, the surface elevation is obtained by solving Eq. (12) explicitly. The time step Δt is adaptive during the simulation, following the Courant–Friedrichs–Lewy (CFL) criterion

$$\Delta t = C \min \left[\min \frac{\Delta x}{|u_{i,j,k}| + \sqrt{gD_{ij}}}, \min \frac{\Delta y}{|v_{i,j,k}| + \sqrt{gD_{ij}}}, \min \frac{\Delta \sigma D_{ij}}{|w_{i,j,k}|} \right] \quad (18)$$

where C is the Courant number, which is taken to be 0.5 to ensure accuracy and stability in the current model.

3.2. Spatial finite volume scheme

We discretize equations (13) and (15) using a second-order Godunov-type finite volume method. It is noticed that applying a standard finite volume Godunov-type scheme directly to the equation does not lead to an automatic preservation of steady state (Zhou et al., 2001; Kim et al., 2008; Liang and Marche, 2009). Therefore, It is desirable to reformulate the equation so that the flux and source terms can be automatically balanced at the discrete level in the steady state. In this study, the method by Liang and Marche (2009) is employed. Taking the x component source term as an example, notice that the total water depth is $D = h + \eta$. The source term can be rewritten as

$$g(h + \eta) \frac{\partial h}{\partial x} = \frac{\partial}{\partial x} \left(\frac{1}{2} g h^2 \right) + g \eta \frac{\partial h}{\partial x} \quad (19)$$

in which the first term in the right hand side can be combined together with the flux terms.

Based on this, the flux and source terms may be expressed as

$$\mathbf{F} = \begin{pmatrix} Duu + \frac{1}{2} g \eta^2 + g h \eta \\ Du v \\ Du w \end{pmatrix} \quad \mathbf{G} = \begin{pmatrix} Du v \\ D v v + \frac{1}{2} g \eta^2 + g h \eta \\ D v w \end{pmatrix} \quad \mathbf{S}_h = \begin{pmatrix} g \eta \frac{\partial h}{\partial x} \\ g \eta \frac{\partial h}{\partial y} \\ 0 \end{pmatrix}$$

The main advantage of the above formulation is that the flux and source terms are well-balanced so that no artificial flow due to bottom slope will be generated.

To solve Eqs. (13) and (15), fluxes based on the conservative variables are required at the cell faces. In high-order Godunov-type methods, the values of the conservative variables within a cell are calculated using a reconstruction method based on the cell center data (Zhou et al., 2001). Usually a piecewise linear reconstruction is used, leading to a second order scheme. For \mathbf{U} in the cell i , we have

$$\mathbf{U} = \mathbf{U}_i + (x - x_i) \Delta \mathbf{U}_i \quad (20)$$

where $\Delta \mathbf{U}_i$ is the gradient of \mathbf{U} , which is calculated by

$$\Delta \mathbf{U}_i = \text{avg} \left(\frac{\mathbf{U}_{i+1} - \mathbf{U}_i}{x_{i+1} - x_i}, \frac{\mathbf{U}_i - \mathbf{U}_{i-1}}{x_i - x_{i-1}} \right) \quad (21)$$

in which avg is a slope limiter which is used to avoid spurious oscillations in the reconstruction data at the cell faces. In this study, the van Leer limiter is adopted, which is given by

$$\text{avg}(a, b) = \frac{a|b| + |a|b}{|a| + |b|} \quad (22)$$

The left and right values of \mathbf{U} at cell face $(i + \frac{1}{2})$ are given by

$$\mathbf{U}_{i+\frac{1}{2}}^L = \mathbf{U}_i + \frac{1}{2} \Delta x_i \Delta \mathbf{U}_i \quad \mathbf{U}_{i+\frac{1}{2}}^R = \mathbf{U}_{i+1} - \frac{1}{2} \Delta x_{i+1} \Delta \mathbf{U}_{i+1} \quad (23)$$

The flux $\mathbf{F}(\mathbf{U}^L, \mathbf{U}^R)$ is calculated by solving a local Riemann problem at each horizontally-facing cell face. In the present study, HLL Riemann solver is employed. The flux at the cell interface $(i + \frac{1}{2})$ is determined by

$$\mathbf{F}(\mathbf{U}^L, \mathbf{U}^R) = \begin{cases} \mathbf{F}(\mathbf{U}^L) & \text{if } s_L \geq 0 \\ \mathbf{F}^*(\mathbf{U}^L, \mathbf{U}^R) & \text{if } s_L < 0 < s_R \\ \mathbf{F}(\mathbf{U}^R) & \text{if } s_R \leq 0 \end{cases} \quad (24)$$

where

$$\mathbf{F}^*(\mathbf{U}^L, \mathbf{U}^R) = \frac{s_R \mathbf{F}(\mathbf{U}^L) - s_L \mathbf{F}(\mathbf{U}^R) + s_L s_R (\mathbf{U}^R - \mathbf{U}^L)}{s_R - s_L} \quad (25)$$

with wave speed s_L and s_R defined by

$$s_L = \min(u^L - \sqrt{g D_L}, u_s - \sqrt{g D_s}) \quad (26)$$

$$s_R = \max(u^R + \sqrt{g D_R}, u_s + \sqrt{g D_s}) \quad (27)$$

where u_s and $\sqrt{g D_s}$ are estimated by

$$u_s = \frac{1}{2} (u^L + u^R) + \sqrt{g D_L} - \sqrt{g D_R} \quad (28)$$

$$\sqrt{g D_s} = \frac{\sqrt{g D_L} + \sqrt{g D_R}}{2} + \frac{u^L - u^R}{4} \quad (29)$$

To obtain the non-hydrostatic velocity field, the dynamic pressure p has to be calculated first. From Eqs. (14) and (16), we get

$$u^{(k)} = u^* - \frac{\Delta t}{\rho} \left(\frac{\partial p}{\partial x} + \frac{\partial p}{\partial \sigma} \frac{\partial \sigma}{\partial x^*} \right)^{(k)} \quad (30)$$

$$v^{(k)} = v^* - \frac{\Delta t}{\rho} \left(\frac{\partial p}{\partial y} + \frac{\partial p}{\partial \sigma} \frac{\partial \sigma}{\partial y^*} \right)^{(k)} \quad (31)$$

$$w^{(k)} = w^* - \frac{\Delta t}{\rho} \frac{1}{D^{(k)}} \frac{\partial p^{(k)}}{\partial \sigma} \quad (32)$$

where $k=1,2$ represents the k th stage in the Runge-Kutta integration.

Applying Eqs. (3) and (4), the continuity Eq. (1) is transformed as

$$\frac{\partial u}{\partial x} + \frac{\partial u}{\partial \sigma} \frac{\partial \sigma}{\partial x^*} + \frac{\partial v}{\partial y} + \frac{\partial v}{\partial \sigma} \frac{\partial \sigma}{\partial y^*} + \frac{1}{D} \frac{\partial w}{\partial \sigma} = 0 \quad (33)$$

Substituting Eqs. (30)–(32) into (33), we obtain the Poisson equation in (x, y, σ) coordinate system

$$\begin{aligned} & \frac{\partial}{\partial x} \left[\frac{\partial p}{\partial x} + \frac{\partial p}{\partial \sigma} \frac{\partial \sigma}{\partial x^*} \right] + \frac{\partial}{\partial y} \left[\frac{\partial p}{\partial y} + \frac{\partial p}{\partial \sigma} \frac{\partial \sigma}{\partial y^*} \right] + \frac{\partial}{\partial \sigma} \left(\frac{\partial p}{\partial x} \right) \frac{\partial \sigma}{\partial x^*} + \frac{\partial}{\partial \sigma} \left(\frac{\partial p}{\partial y} \right) \frac{\partial \sigma}{\partial y^*} \\ & + \left[\left(\frac{\partial \sigma}{\partial x^*} \right)^2 + \left(\frac{\partial \sigma}{\partial y^*} \right)^2 + \frac{1}{D^2} \right] \frac{\partial}{\partial \sigma} \left(\frac{\partial p}{\partial \sigma} \right) \\ & = \frac{\rho}{\Delta t} \left(\frac{\partial u^*}{\partial x} + \frac{\partial u^*}{\partial \sigma} \frac{\partial \sigma}{\partial x^*} + \frac{\partial v^*}{\partial y} + \frac{\partial v^*}{\partial \sigma} \frac{\partial \sigma}{\partial y^*} + \frac{1}{D} \frac{\partial w^*}{\partial \sigma} \right) \end{aligned} \quad (34)$$

The above equation is discretized with the second-order space-centered finite difference method. The velocities of (u^*, v^*, w^*) at vertical cell faces are interpolated from adjacent cell-centered values. The resulting linear equation is given by

$$\begin{aligned} & a_1 p_{i-1,k-1} + a_2 p_{i-1,j,k-1} + a_3 p_{i,j,k-1} + a_4 p_{i+1,j,k-1} + a_5 p_{i,j+1,k-1} + a_6 p_{i,j-1,k} \\ & + a_7 p_{i-1,j,k} + a_8 p_{i,j,k} + a_9 p_{i+1,j,k} + a_{10} p_{i,j+1,k} + a_{11} p_{i,j-1,k+1} \\ & + a_{12} p_{i-1,j,k+1} + a_{13} p_{i,j,k+1} + a_{14} p_{i+1,j,k+1} + a_{15} p_{i,j+1,k+1} = R_p \end{aligned} \quad (35)$$

where

$$\begin{aligned} a_1 &= - \left(\frac{(\sigma_y)_{ij-1,k}}{2 \Delta y (\Delta \sigma_k + \Delta \sigma_{k-1})} + \frac{(\sigma_y)_{i,j,k}}{2 \Delta y (\Delta \sigma_k + \Delta \sigma_{k-1})} \right) \\ a_2 &= - \left(\frac{(\sigma_x)_{i-1,j,k}}{2 \Delta x (\Delta \sigma_k + \Delta \sigma_{k-1})} + \frac{(\sigma_x)_{i,j,k}}{2 \Delta x (\Delta \sigma_k + \Delta \sigma_{k-1})} \right) \\ a_3 &= - \frac{(\sigma_x^2 + \sigma_y^2 + \frac{1}{D^2})_{i,j,k}}{0.5 (\Delta \sigma_k + \Delta \sigma_{k-1}) \Delta \sigma_{k-1}} \\ a_4 &= \frac{(\sigma_x)_{i+1,j,k}}{2 \Delta x (\Delta \sigma_k + \Delta \sigma_{k-1})} + \frac{(\sigma_x)_{i,j,k}}{2 \Delta x (\Delta \sigma_k + \Delta \sigma_{k-1})} \\ a_5 &= \frac{(\sigma_y)_{i,j+1,k}}{2 \Delta y (\Delta \sigma_k + \Delta \sigma_{k-1})} + \frac{(\sigma_y)_{i,j,k}}{2 \Delta y (\Delta \sigma_k + \Delta \sigma_{k-1})} \\ a_6 &= a_{10} = - \frac{1}{\Delta y^2} \quad a_7 = a_9 = - \frac{1}{\Delta x^2} \\ a_8 &= \frac{2}{\Delta x^2} + \frac{2}{\Delta y^2} + \frac{(\sigma_x^2 + \sigma_y^2 + \frac{1}{D^2})_{i,j,k}}{0.5 (\Delta \sigma_k + \Delta \sigma_{k-1}) \Delta \sigma_{k-1}} + \frac{(\sigma_x^2 + \sigma_y^2 + \frac{1}{D^2})_{i,j,k}}{0.5 (\Delta \sigma_k + \Delta \sigma_{k-1}) \Delta \sigma_{k-1}} \\ a_{11} &= \frac{(\sigma_y)_{i,j-1,k}}{2 \Delta y (\Delta \sigma_k + \Delta \sigma_{k-1})} + \frac{(\sigma_y)_{i,j,k}}{2 \Delta y (\Delta \sigma_k + \Delta \sigma_{k-1})} \\ a_{12} &= \frac{(\sigma_x)_{i-1,j,k}}{2 \Delta x (\Delta \sigma_k + \Delta \sigma_{k-1})} + \frac{(\sigma_x)_{i,j,k}}{2 \Delta x (\Delta \sigma_k + \Delta \sigma_{k-1})} \\ a_{13} &= - \frac{(\sigma_x^2 + \sigma_y^2 + \frac{1}{D^2})_{i,j,k}}{0.5 (\Delta \sigma_k + \Delta \sigma_{k-1}) \Delta \sigma_k} \\ a_{14} &= - \left(\frac{(\sigma_x)_{i+1,j,k}}{2 \Delta x (\Delta \sigma_k + \Delta \sigma_{k-1})} + \frac{(\sigma_x)_{i,j,k}}{2 \Delta x (\Delta \sigma_k + \Delta \sigma_{k-1})} \right) \\ a_{15} &= - \left(\frac{(\sigma_y)_{i,j+1,k}}{2 \Delta y (\Delta \sigma_k + \Delta \sigma_{k-1})} + \frac{(\sigma_y)_{i,j,k}}{2 \Delta y (\Delta \sigma_k + \Delta \sigma_{k-1})} \right) \\ R_p &= - \frac{\rho}{\Delta t} \left(\frac{\partial u^*}{\partial x} + \frac{\partial u^*}{\partial \sigma} \frac{\partial \sigma}{\partial x^*} + \frac{\partial v^*}{\partial y} + \frac{\partial v^*}{\partial \sigma} \frac{\partial \sigma}{\partial y^*} + \frac{1}{D} \frac{\partial w^*}{\partial \sigma} \right) \end{aligned}$$

where $\sigma_x = \frac{\partial \sigma}{\partial x^*}$ and $\sigma_y = \frac{\partial \sigma}{\partial y^*}$.

Uniform gridding is used in the horizontal direction while gridding in the vertical direction is generalized to be non-uniform in order to capture the bottom and surface boundary layers when desired. The coefficient matrix is asymmetric and has a total of 15 diagonal lines. The linear system is solved using the high performance preconditioner HYPRE software library. With p solved, the non-hydrostatic velocities at each stage can be updated from Eqs. (30)–(32).

3.3. Boundary conditions

To solve the governing equations, boundary conditions are required for all the physical boundaries. At the free surface, the continuity of normal and tangential stresses is enforced. With wind effects absent, the tangential stress equals zero, resulting in

$$\frac{\partial u}{\partial \sigma} \Big|_{z=\eta} = \frac{\partial v}{\partial \sigma} \Big|_{z=\eta} = 0 \quad (36)$$

The vertical velocity w at the ghost cells is obtained to ensure that w at free surface satisfies the kinematic boundary condition

$$w|_{z=\eta} = \frac{\partial \eta}{\partial t} + u \frac{\partial \eta}{\partial x} + v \frac{\partial \eta}{\partial y} \quad (37)$$

The zero pressure condition on the free surface is applied when the Poisson equation is solved

$$p|_{z=\eta} = 0 \quad (38)$$

At the bottom, the normal velocity and the tangential stress are prescribed. The normal velocity w is imposed through the kinematic boundary condition

$$w|_{z=-h} = -\frac{\partial h}{\partial t} - u \frac{\partial h}{\partial x} - v \frac{\partial h}{\partial y} \quad (39)$$

For the horizontal velocities, either free-slip boundary conditions

$$\frac{\partial u}{\partial \sigma} \Big|_{z=-h} = \frac{\partial v}{\partial \sigma} \Big|_{z=-h} = 0 \quad (40)$$

or bottom shear stresses are considered

$$v_t \frac{\partial \mathbf{u}}{\partial \sigma} \Big|_{z=-h} = Dc_d |\mathbf{u}_b| \mathbf{u}_b \quad (41)$$

where c_d is the bed drag coefficient, which can be computed from the law of the wall for fully rough, turbulent flow as $c_d = 0.16 [ln^2(15\Delta z_1/k_s)]^{-2}$, $\Delta z_1 = D\Delta\sigma_1$ is the thickness of the cell above the bed, k_s is the bottom roughness height. \mathbf{u}_b is velocity at the cell above the bed.

The Neumann boundary condition is used for dynamic pressure, which is directly obtained from the governing equation for w

$$\frac{\partial p}{\partial \sigma} \Big|_{z=-h} = -\rho D \frac{dw}{dt} \Big|_{z=-h} \quad (42)$$

where w at $z = -h$ is given by (39). In the application to an underwater landslide in Section 4.6 below, we linearize the resulting boundary condition which gives

$$\frac{\partial p}{\partial \sigma} \Big|_{z=-h} = \rho D \frac{\partial^2 h}{\partial t^2} \quad (43)$$

At the closed boundaries or vertical walls, free-slip boundary conditions are imposed, so that the normal velocity and the tangential stress are set to zero. The normal pressure gradient is zero. At inflow, both free surface and velocities calculated from the analytical solutions are specified. In the lateral direction, periodic boundary conditions can be applied. To facilitate the parallel implementation, we used two ghost cells at each boundaries. The boundary conditions are specified at the ghost cells.

3.4. Wetting–drying treatment

It is straightforward to use a wetting–drying scheme for modeling moving boundaries. In the present study, a simple wetting–drying scheme is implemented. The wet and dry cells are judged by total water depth D . If a cell has the total water depth D greater than D_{min} , it is a wet cell with $Mask_{ij} = 1$. Otherwise it is a dry cell with $Mask_{ij} = 0$. D_{min} is the minimum water depth allowed for computation. The surface elevation in the dry cells are defined as $\eta_{ij} = D_{min} - h_{ij}$. For a dry cell surrounded by wet cells, $Mask_{ij}$ has to be reevaluated as

$$\begin{aligned} Mask_{ij} &= 1 & \text{if } \eta_{ij} \leq \eta_{neighbor} \\ Mask_{ij} &= 0 & \text{if } \eta_{ij} > \eta_{neighbor} \end{aligned} \quad (44)$$

In the dry cells, the normal flux at cell faces are set to zero. The wave speed of Eqs. (26) and (27) for a dry bed are modified as (Zhou et al., 2001)

$$s_L = u^L - \sqrt{gD_L} \quad s_R = u^L + 2\sqrt{gD_L} \quad (\text{right dry bed}) \quad (45)$$

$$s_L = u^R - 2\sqrt{gD_R} \quad s_R = u^R + \sqrt{gD_R} \quad (\text{left dry bed}) \quad (46)$$

4. Numerical results

The numerical method presented in the above section has been tested with several analytical solutions and laboratory experiments. Seven test cases are given in this section: (1) standing wave in closed basin; (2) solitary wave propagation in constant depth; (3) periodic wave over submerged bar; (4) wave transformation over an elliptical shoal on a sloped bottom; (5) breaking solitary wave runup; (6) tsunami generation by three-dimensional rigid underwater landslides; and (7) longshore current on a plane beach. These test cases have been widely used to validate non-hydrostatic models.

4.1. Standing wave in closed basin

The numerical model was first tested by the analytical solution of a standing wave in closed basin with length of $L = 20$ m and depth of $D = 10$ m. This test case has been studied by various researchers, for example, Casulli and Stelling (1998), Casulli (1999) and Chen (2003). They used more than 20 vertical layers in order to correctly simulate wave dispersion. With Keller-box scheme, Stelling and Zijlema (2003) obtained good agreement with analytical solution by using two layers. These models are all solved in Cartesian coordinate system. In this section, we will show that the present model in σ coordinates can reproduce accurate waves with relatively few vertical layers.

The initial surface elevation is given by

$$\eta = a \cos\left(\frac{\pi x}{10}\right) \quad (47)$$

where η is the surface elevation in meters, $a = 0.1$ m is the amplitude of the standing wave. The wave length equals the length of the basin. Since $kD = \pi > 1$, the wave is highly dispersive. From the dispersion relationship $\sigma^2 = gk \tanh(kD)$, where $\sigma = 2\pi/T$, $k = 2\pi/L$, we can calculate wave period $T = 3.59$ s. The linearized analytical solution for this standing wave is

$$\eta = a \cos(kx) \cos(\sigma t) \quad (48)$$

For the numerical setup, a uniform grid spacing of 0.2 m was used in the horizontal direction. This is a finely resolved horizontal mesh corresponding to 100 grid cells per wavelength. Hence one does not expect large discretization errors due to the horizontal grid effects. In the vertical direction, five layers are employed. Fig. 2 shows the comparisons of numerical and analytical surface elevations at $x = 0.1$ m and $x = 17.5$ m. The computed surface eleva-

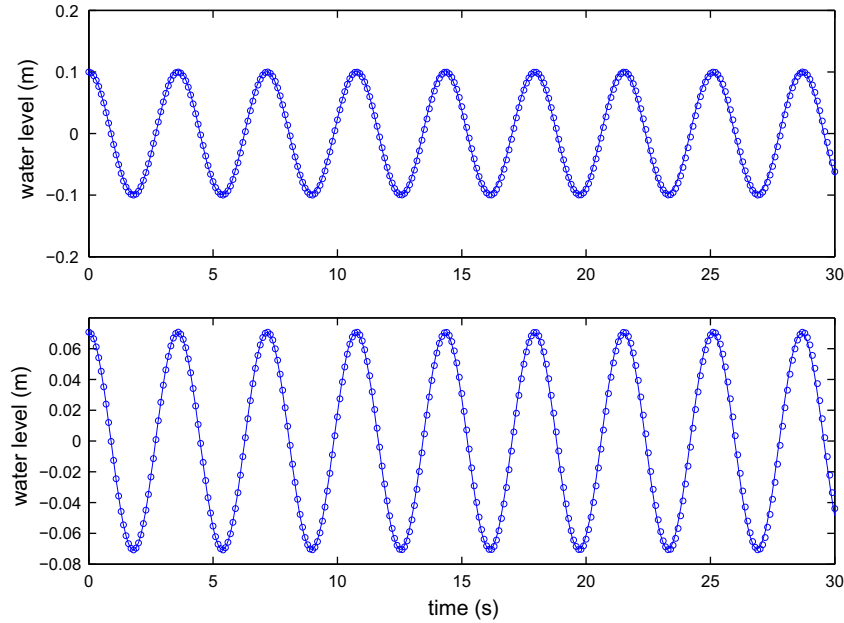


Fig. 2. Comparisons between numerical (solid line) and analytical (circles) surface elevations at $x = 0.1$ m (upper panel) and $x = 17.5$ m (lower panel) for the standing wave in closed basin.

tions agree very well with the analytical solution. The amplitude of the wave has no significant change. Fig. 3 gives the normalized root-mean square errors at $x = 17.5$ m as a function of the number of vertical layers and wave dispersion parameter kD , which is obtained by varying water depth D . The numerical error is defined as $error = \frac{1}{H} \sqrt{\frac{1}{N} \sum_{j=1}^N (\eta_a - \eta_j)^2}$, where N is the number of data that are compared, η_a is the analytical solution, H is the wave height at $x = 17.5$ m. The simulation time is 30 s. As expected, the numerical errors are decreased by increasing the number of vertical layers. The numerical results are less accurate for higher dispersive wave with the same vertical layers. Therefore, more vertical layers are required to obtain sufficiently accurate predictions for highly dispersive waves.

4.2. Solitary wave propagation in constant depth

The second test case is the solitary wave propagation in constant water depth. The computational domain is two-dimensional

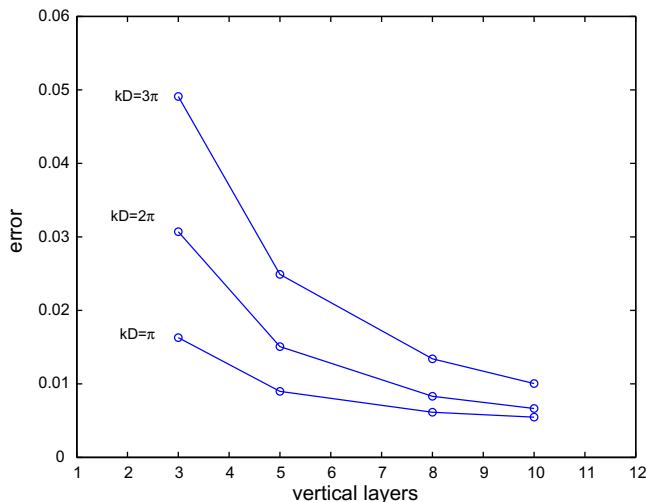


Fig. 3. Numerical errors at $x = 17.5$ m as a function of the number of vertical layers and wave dispersion parameter kD .

with length of 200 m and water depth of 1.0 m. The solitary wave is initially at $x = 8.0$ m. An exact solution of the fully nonlinear equations, obtained using Tanaka's (1986) method, was used to specify the initial surface elevation and velocity field ($t = 0$ s at Figs. 4 and 5). The solitary wave has the wave height to the still water depth ratio $H/h = 0.5$, indicating that the solitary wave is highly nonlinear. The domain is discretized by a uniform grid in the horizontal direction with $\Delta x = 0.1$ m and three layers in the vertical direction. The time step Δt is adjusted during the simulation based on the Courant number, which is taken as 0.5.

Fig. 4 shows the comparisons of simulated surface elevations and Tanaka solutions at $t = 10, 20, 40$ s. We can see that the agreements are almost perfect. As the wave propagates to the right, the wave shape hardly change. Fig. 5 shows the comparisons of horizontal and vertical velocities at the middle elevation between numerical results and Tanaka solutions (Tanaka, 1986). The good agreement of vertical velocity indicates that the dynamic pressure has been well simulated by the model with three vertical layers. To quantitatively assess the comparisons, we calculate the relatively error $|(\phi_{comp} - \phi_{ana})/\phi_{ana}|$, where ϕ is the peak value of surface elevation and velocities. At $t = 40$ s, the relatively errors for surface elevation η , horizontal velocity u and vertical velocity w are 2.7%, 2.6% and 0.8%, respectively. These relatively small errors indicate that the solitary wave is rarely decayed by the numerical diffusion.

4.3. Periodic wave over submerged bar (Beji and Battjes, 1993)

In this section, the model is applied to simulate wave shoaling over a submerged bar. The experimental data by Beji and Battjes (1993) is used to validate our non-hydrostatic model. This case has been used to verify a number of non-hydrostatic free surface models including Casulli (1999), Lin and Li (2002), Chen (2003), Stelling and Zijlema (2003), Yuan and Wu (2004a,b) and Bradford (2005). The data has also frequently been used as a test of Boussinesq models, as the case falls outside the range of typical $O(\mu^2)$ models such as Wei et al. (1995), but is handled by various higher order approaches such as Gobbi and Kirby (1999) or Lynett and Liu (2002).

The model setup and bottom geometry is shown in Fig. 6. The wave flume has a length of 30 m. The still water depth is 0.4 m,

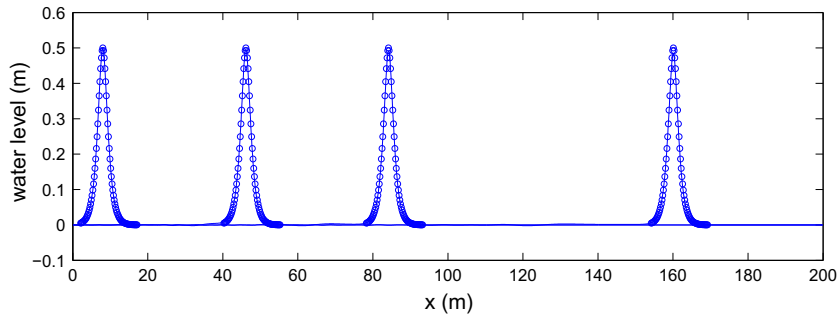


Fig. 4. Comparisons between simulated surface elevations (solid line) and Tanaka solutions (circles) at $t = 0, 10, 20, 40$ s for solitary wave propagation in constant depth.

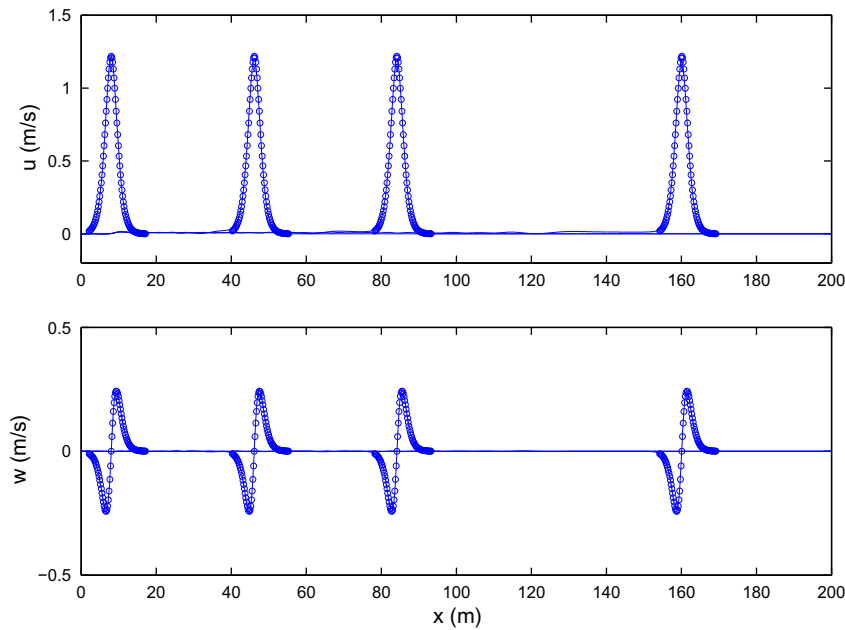


Fig. 5. Comparisons between simulated velocities (solid line) and Tanaka solutions (circles) at $t = 0, 10, 20, 40$ s for solitary wave propagation in constant depth.

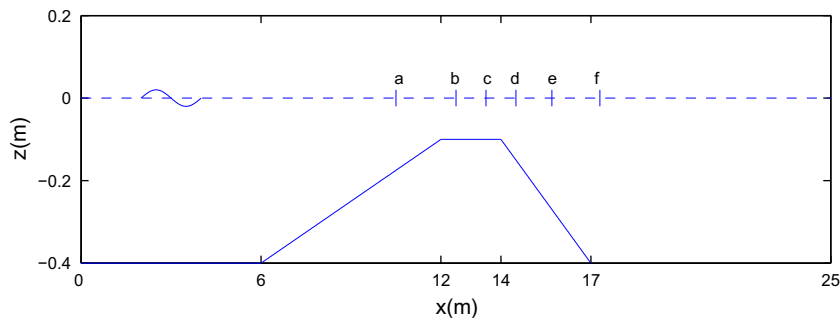


Fig. 6. Bottom geometry and location of wave gauges used in the computation (a) $x = 10.5$ m; (b) $x = 12.5$ m; (c) $x = 13.5$ m; (d) $x = 14.5$ m; (e) $x = 15.7$ m; (f) $x = 17.3$ m.

which is reduced to 0.1 m at the bar. The offshore slope of the bar is $1/20$ and the onshore slope is $1/10$. Periodic waves with period 2.02 s and amplitude 1.0 cm are incident at the left boundary. The computational domain is 35 m long with 10 m of sponge layer at the right end. The sponge layer technique introduced by Larsen and Dancy (1983) is employed. This technique has been widely used to absorbing shortwaves (Chen et al., 1999). To discretize the computational domain, 1750 constant horizontal grids and three vertical layers are used to ensure that the free higher harmonics can be properly calculated.

Fig. 7 shows the comparisons of free surface elevation at six measurement locations between numerical results and experimental data. Wave shoaling at station a and propagation over the bar at station b are well simulated by the model. The bound higher harmonics generated by the nonlinear shoaling wave on the upward slope of the bar become free on the downward slope, resulting in irregular wave pattern at station c–f. The model generally predicts free surface evolution at these stations well, indicating that the dispersion for higher frequency components is well simulated with three vertical layers.

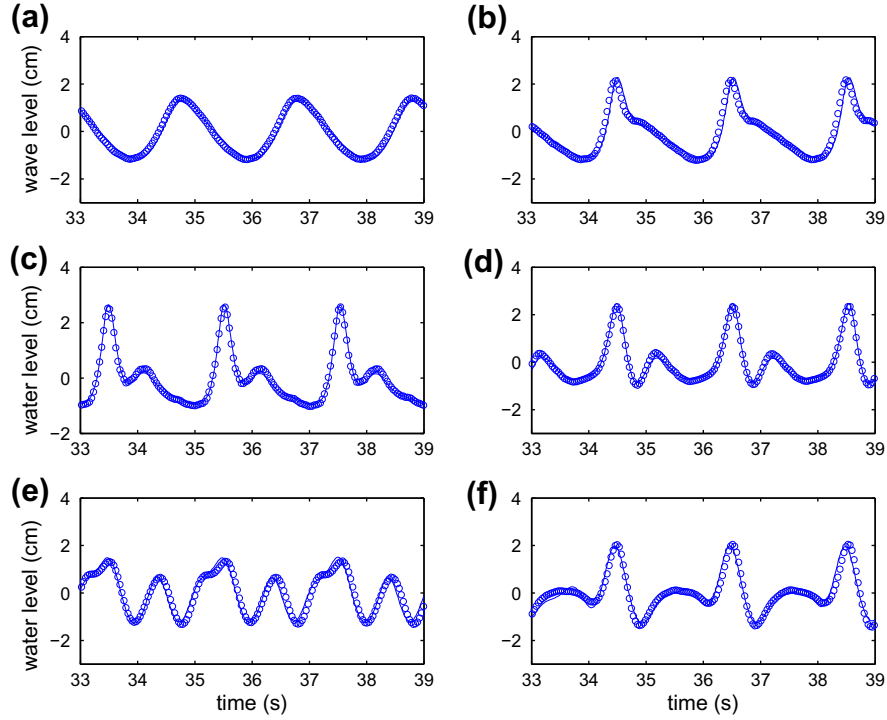


Fig. 7. Comparisons between numerical (solid line) and experimental (circles) surface elevations at (a) $x = 10.5$ m; (b) $x = 12.5$ m; (c) $x = 13.5$ m; (d) $x = 14.5$ m; (e) $x = 15.7$ m; (f) $x = 17.3$ m.

4.4. Wave transformation over an elliptical shoal on a sloped bottom

This example is to test the model's capability of simulating wave refraction and diffraction over a 3D uneven bottom. The corresponding experiment was conducted by Berkhoff et al. (1982). The model setup and bottom geometry is shown in Fig. 8. An elliptical shoal is located on a plane beach with a slope of 1/50. Let (x', y') be the slope-oriented coordinates, which are related to (x, y) coordinate system by means of rotation over -20° . The still water depth without shoal is given by

$$\begin{aligned} h &= 0.45 \quad x' < -5.84 \\ h &= \max(0.07, 0.45 - 0.02(5.84 + x')) \quad x' \geq -5.84 \end{aligned} \quad (49)$$

Since the minimum water depth is 0.07 m, the wave is non-breaking. The boundary of the shoal is given by

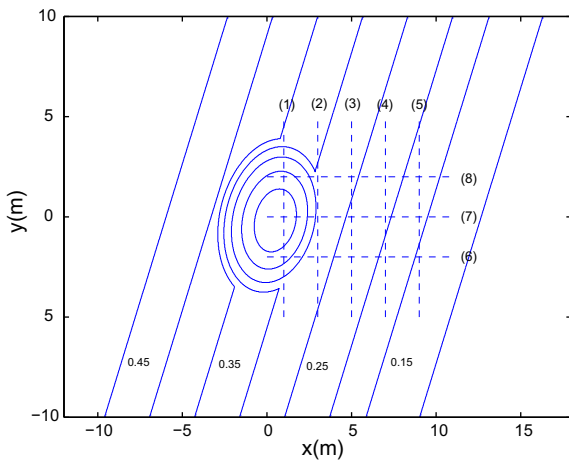


Fig. 8. Bottom geometry for periodic wave propagation over an elliptical shoal, experimental setup by Berkhoff et al. (1982).

$$\left(\frac{x'}{3}\right)^2 + \left(\frac{y'}{4}\right)^2 = 1 \quad (50)$$

where the thickness of the shoal is

$$d = -0.3 + 0.5\sqrt{1 - \left(\frac{x'}{3.75}\right)^2 - \left(\frac{y'}{5}\right)^2} \quad (51)$$

Regular wave with wave period of 1.0 s and wave height of 4.64 cm are incident at the left boundary $x = -12$ m. At the right end, waves are completely absorbed by a sponge layer with $L = 5$ m. Two walls are located at $y = -10$ m and 10 m, where free-slip boundary conditions are imposed.

To well simulate wave refraction and diffraction, a fine grid with $\Delta x = 0.025$ m and $\Delta y = 0.05$ m is used. Five vertical layers are used in the vertical direction. The time step is adjusted during the simulation, with courant number 0.5. The simulation period is 30 s. The final five waves are employed to estimate wave height. To quantitatively assess the model results, we calculate normalized root mean square error $rms = \frac{1}{\bar{X}_{obs}} \sqrt{\frac{1}{N} \sum_{i=1}^N (X_{mod} - X_{obs})^2}$, where X is the variable being compared, mod and obs stand for model results and observations, \bar{X} is mean value. Fig. 9 shows the comparisons of wave height between numerical results and experiment data at eight measurement sections. Due to refraction, wave focusing occurs behind the shoal with a maximum wave height of approximately 2.2 times the incident wave height (around $x = 5$ m, $y = 0$ m). The model slightly under-predicts the peak wave height at Sections 3 and 5. However, the wave height variations along these two section are well captured. The normalized rms errors for both sections are 0.11. In other sections, the predictions agree quite well with the measurements. For example, the normalized rms error at Section 1 is 0.07. These results demonstrate that wave refraction and diffraction can be well simulated by the model.

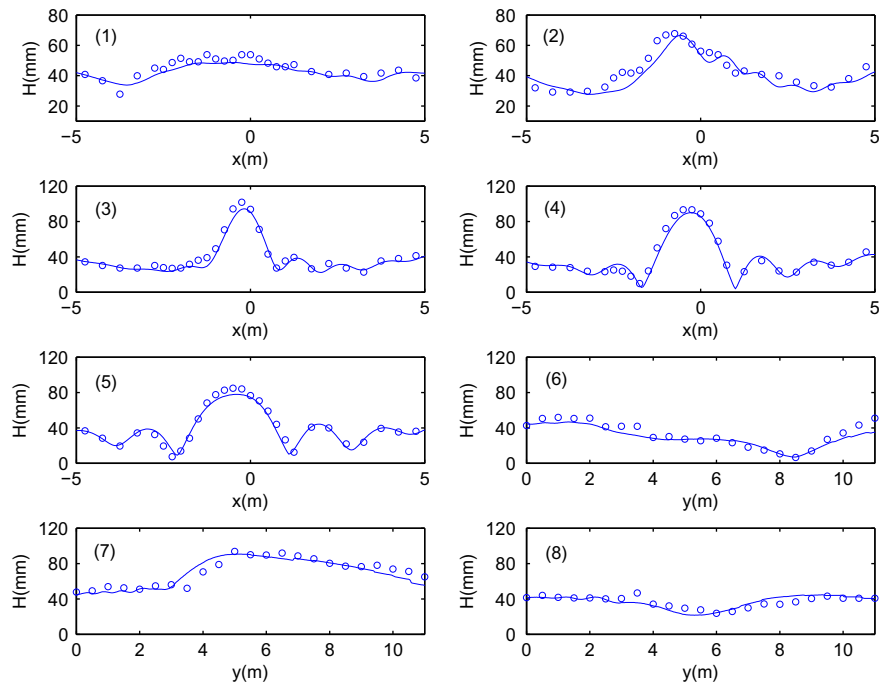


Fig. 9. Comparisons between numerical (solid line) and experimental (circles) wave height at eight stations.

4.5. Breaking solitary wave run-up

To show the model's capability of simulating breaking waves and wetting–drying, we applied the model to study breaking solitary wave run-up and run-down in a slope beach. The corresponding laboratory experiment was conducted by Synolakis (1987). The beach slope is 1/20. The still water depth varies from 0.21 m to 0.29 m. A solitary wave which has a wave height to still water depth ratio of 0.28 was incident on the left. Wave gauges were used to record the free surface displacement during the run-up and run-down.

In the numerical simulation, the solitary wave is initially at 1.5 m on the left from the toe of the beach. An exact solution of the fully nonlinear equations, obtained using Tanaka's (1986) method, was used to specify the initial surface elevation and velocity field, see Fig. 10. The computational domain extends to a location beyond the maximum run-up point. The entire domain is discretized by 550 uniform grid in the horizontal with $\Delta x = 0.02$ m. Three layers are used in the vertical direction. The minimum water depth is 5 mm, which determines wetting-and-drying of the computational cells.

The numerical results were compared with the experimental data after normalization. The length scale is normalized by the still

water depth d and the time scale is normalized by $\sqrt{g/d}$. Fig. 11 shows comparisons of simulated and measured free surface profile during wave shoaling, breaking, run-up and run-down. Panels (a) and (b) show the shoaling process of the solitary wave. The wave becomes more asymmetric and the wave height increases as water depth decreases. Around $t\sqrt{g/d} = 20$, the wave starts to break as shown in panel (c), the surface profile is dramatically changed and the wave height is rapidly reduced. The wave continuously breaks as its turbulent front moves towards the shoreline. After the wave front passes the still-water shoreline, it collapses and the consequent run-up process commences. The run-up process is shown in the panel (d) and (e). After reaching the maximum run-up point, the front starts to run-down which is shown in the panel (f). The comparisons between the simulation and experiment data are fairly good. The shoaling, breaking, run-up and run-down processes of the solitary wave are well reproduced. In Fig. 11, we also shown the numerical results without turbulent diffusion terms. During wave shoaling and breaking (panel (a)–(c)), the predicted surface elevation is seldom impacted by neglecting turbulence diffusion. The shock-capturing scheme employed in the model can well describe the initiation of wave breaking process. However, the model without turbulence dissipation slightly over-predicts wave run-up as shown in panel (e) and (f). Generally,

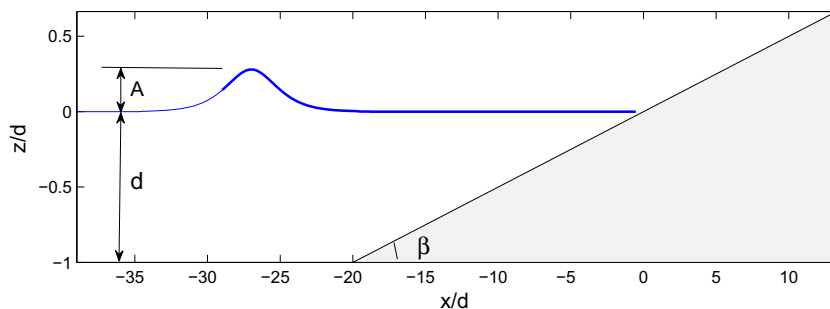


Fig. 10. Computational domain and model setup. The beach slope is 1/20. The still water depth is 0.21 m. The amplitude of solitary wave is 0.0588 m.

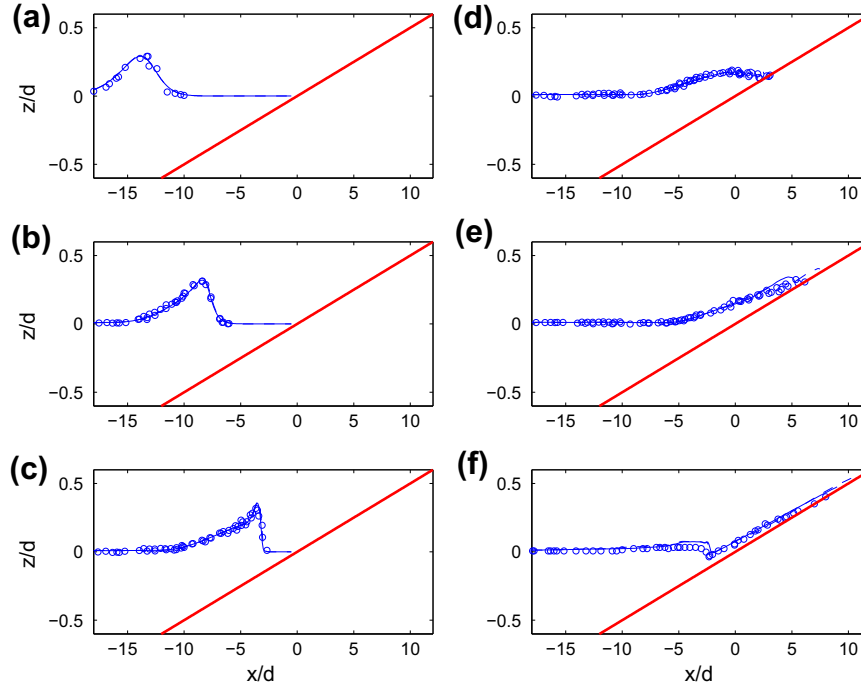


Fig. 11. Comparisons between numerical (with subgrid model: solid line; without subgrid model: dashed line) and experimental (circles) free surface elevation for breaking solitary wave run-up and run-down at (a) $t\sqrt{g/d} = 10$; (b) $t\sqrt{g/d} = 15$; (c) $t\sqrt{g/d} = 20$; (d) $t\sqrt{g/d} = 25$; (e) $t\sqrt{g/d} = 30$; (f) $t\sqrt{g/d} = 50$.

neglecting turbulence had little impact on the predicted surface elevations, which have been found by Bradford (2011) and Zijlema and Stelling (2008), who successfully simulated breaking waves with Euler equations.

4.6. Tsunami generation by three-dimensional underwater landslides

Submarine landslides are one of the most dangerous mechanisms for tsunami generation in the coastal areas. In this section, we applied the model to simulate tsunami generation by an idealized three-dimensional underwater landslides. Experiments have recently been performed by Enet and Grilli (2007) in a 3.7 m wide, 1.8 m deep and 30 m long wave tank with a plane underwater slope with $\theta = 15^\circ$ angle. This data set has also been used recently by Fuhrman and Madsen (2009) to test the accuracy of a higher-order Boussinesq model.

The vertical cross section of the landslide is shown in Fig. 12. The geometry is defined using truncated hyperbolic secant functions

$$\zeta = \frac{T}{1-\epsilon} [\text{sech}(k_b x) \text{sech}(k_w y) - \epsilon] \quad (52)$$

where $k_b = 2C/b$, $k_w = 2C/w$ and $C = \text{acosh}(1/\epsilon)$. The landslide has length $b = 0.395$ m, width $w = 0.680$ m and thickness $T = 0.082$ m. The truncation parameter $\epsilon = 0.717$. The landslide is initially located at the submergence depth d . The movement of the landslide is prescribed as

$$s(t) = s_0 \ln \left(\cosh \frac{t}{t_0} \right) \quad (53)$$

which closely approximates the landslide displacement measured in experiments. s_0 and t_0 are given by

$$s_0 = \frac{u_t^2}{a_0}, \quad t_0 = \frac{u_t}{a_0} \quad (54)$$

where u_t and a_0 are the landslide terminal velocity and initial acceleration, respectively. To represent the landslide, the horizontal domain is discretized by a uniform grid with $\Delta x = 0.02$ m and $\Delta y = 0.02$ m. Three vertical layers are employed in the simulation. The landslide parameters are $u_t = 1.70$ m/s and $a_0 = 1.12$ m/s².

Three wave gauges are located at (x, y) locations (1469, 350), (1929, 0) and (1929, 500), where all distances are in mm and where x denotes distance from the still water shoreline and y denotes dis-

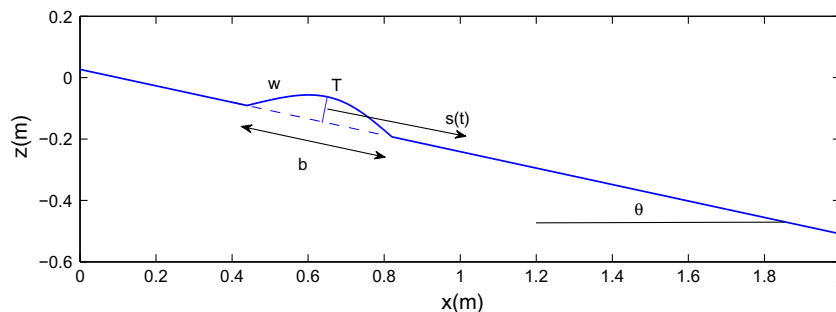


Fig. 12. Vertical cross section for numerical setup of tsunami landslide. The gaussian shape landslide model has length $b = 0.395$ m, width $w = 0.680$ m and thickness $T = 0.082$ m and is initially located at submergence depth d . The beach slope has an angle of $\theta = 15^\circ$.

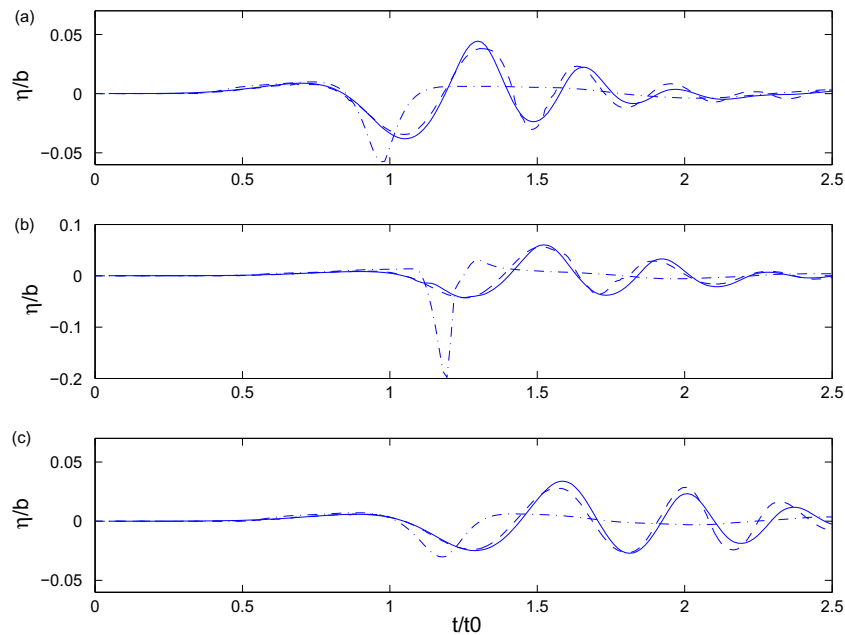


Fig. 13. Comparisons between nonhydrostatic numerical results (solid lines), hydrostatic numerical results (dash-dot lines) and experimental data (dashed lines) for free surface elevation for landslide-generated waves at three wave gauges with initial depth of submergence $d = 61$ mm. Gauge coordinates (x, y) : (a) (1469, 350) mm; (b) (1929, 0) mm; (c) (1929, 500) mm, where x is distance from shoreline and y is perpendicular distance from the axis of the shore-normal slide trajectory.

tances off the centerline axis of the sliding mass. Model results are presented as time series in comparison to measured data at each of the three gages, with two representative tests chosen. Fig. 13 shows model/data comparisons for the case of an initial submergence of the landslide center of $d = 61$ mm. The model is seen to represent the amplitude and the phase structure of the generated wave train well. As would be expected, wave heights are highest at the gage lying along the axis of the landslide motion and drop off with distance away from the centerline axis. Fig. 13 also displays the results of a hydrostatic model simulation, which are obtained by neglecting the pressure correction steps indicated in Eqs. (14) and (16). These results are markedly different from the nonhydrostatic model results, indicating the great importance of dispersion in this test. The hydrostatic result basically consists of a strong drawdown of the water column immediately behind the sliding mass. This drawdown first grows in magnitude and then decreases as the relative depth of submergence becomes larger. In contrast, the nonhydrostatic model result consists of a packet of dispersive waves which lag behind the relatively faster moving slide as the slide accelerates. This behavior is further illustrated in snapshots of the generated wave trains at times $t = 1, 2$ and 3 s shown in Figs. 14 and 15, with nonhydrostatic behavior shown in the sequence of panels in Fig. 14 and hydrostatic behavior shown in the sequence in Fig. 15. The absence of dispersion in the generated waves in Fig. 15 is clear, emphasizing the importance of frequency dispersion in the present example. We note that the results of Fuhrman and Madsen (2009), obtained using a higher-order Boussinesq model, showed comparable capabilities in predicting wave phase structure as the nonhydrostatic model here, but tended to overpredict crest and trough heights to some degree in comparison to the results here; see their Fig. 14.

Fig. 16 illustrates similar results for the case of an initial depth of submergence of $d = 120$ mm. Generated wave heights are lower here than in the previous case due to the greater depth of submergence, but the pattern of sea surface response is qualitatively similar to the previous case. Hydrostatic results for this case have not been computed as the problem is in relatively deeper water than the previous case.

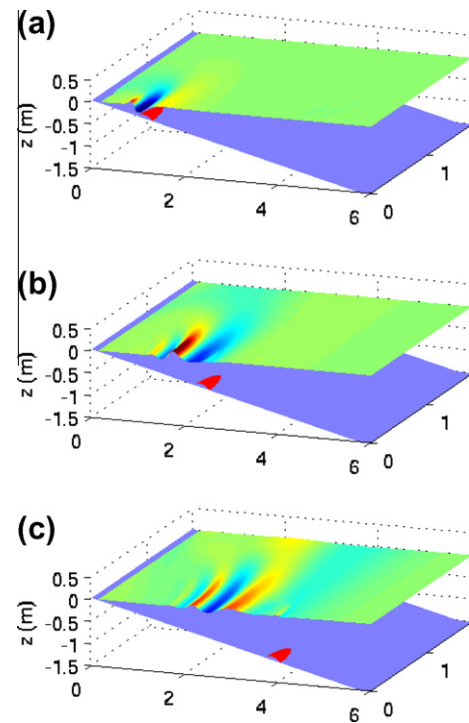


Fig. 14. Snapshots of landslide-generated waves simulated using nonhydrostatic model at times (a) $t = 1.0$ s; (b) $t = 2.0$ s and (c) $t = 3.0$ s after release of the sliding mass. The surface elevation is exaggerated 5 times.

4.7. Longshore current on a plane beach

The implementations of turbulence closure and periodic boundary condition enable us to simulate longshore current in the surf zone. The laboratory measurements of breaking-generated longshore currents on plane beaches reported by Visser (1991) are employed to demonstrate the capability of the model. We particularly

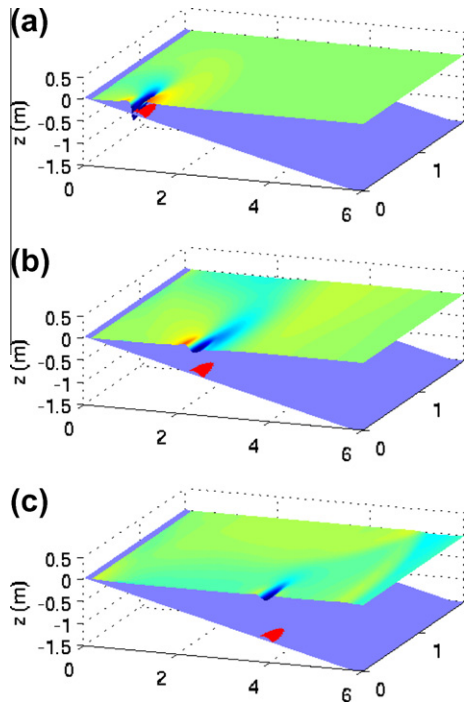


Fig. 15. Snapshots of landslide-generated waves simulated using hydrostatic model at times (a) $t = 1.0$ s; (b) $t = 2.0$ s and (c) $t = 3.0$ s after release of the sliding mass. The surface elevation is exaggerated 5 times.

choose case 4 in Visser's (1991) experiments. This data set has been employed by Chen et al. (2003) to test wave-resolving Boussinesq model. In the physical model, the slope of the smooth concrete beach is 1:20, which starts from an offshore water depth of 35 cm. The obliquely incident, regular wave train has an amplitude of 3.9 cm, with a period of 1.02 s and an angle of incidence of 15.4° in the offshore boundary.

The computational domain is chosen to be 8.4 m long with a 0.6 m flat bottom placed in front of the slope. The width of the do-

main is determined on the basis of periodic lateral boundary condition. The domain is discretized by 280×128 grid cells with $\Delta x = 0.03$ m and $\Delta y = 0.04325$ m. Five vertical layers are used. Turbulence model is turned on to account for wave breaking-induced energy dissipation. The bottom roughness height is chosen as $k_s = 0.08$ cm by tuning the model to match the measurement.

Fig. 17 shows a snapshot of computed surface elevation. Due to the nonlinear shoaling effects, the wave crest becomes narrow and asymmetric near the shoreline. The wave height is greatly reduced by the depth-limited wave breaking. The breaking-generated longshore current is obtained by time-averaging the depth-averaged current over five wave periods, which is demonstrated in Fig. 18. The computed time-averaged flow field is longshore uniform and no shear instabilities occur, which is consistent with the Boussinesq model simulation (Chen et al., 2003). The cross-shore velocity is nearly zero, indicating that the mass is balanced. Fig. 19 gives the comparisons of computed wave setup and longshore current with the laboratory measurements. Generally, the comparisons are quite good. The model slightly underestimates wave setdown near the breaking region. It might be because the breaking wave is a plunging breaker in the laboratory experiment, which cannot be well simulated by the model. The computed longshore current is estimated at $t = 110$ s. We notice that the difference of computed longshore currents at $t = 100$ s and $t = 110$ s is minor, indicating that a steady solution of longshore current has been achieved at the end of simulation. The magnitude and the location of maximum longshore current are well predicted by the model. The correct prediction of cross-shore variation of longshore current indicates that the model can reasonably simulate wave breaking and associated energy dissipation. We also show the computed wave setup and longshore current without turbulent diffusion, which are demonstrated as dash-dotted lines in Fig. 19. The difference of predicted wave set-down with and without turbulent diffusion is minor. The model without turbulent diffusion predicts slightly smaller wave setup inside surf zone. However, the turbulent diffusion has significant effects on the longshore current. Without turbulent diffusion, the longshore current peaks further onshore than that with turbulent diffusion and measurement.

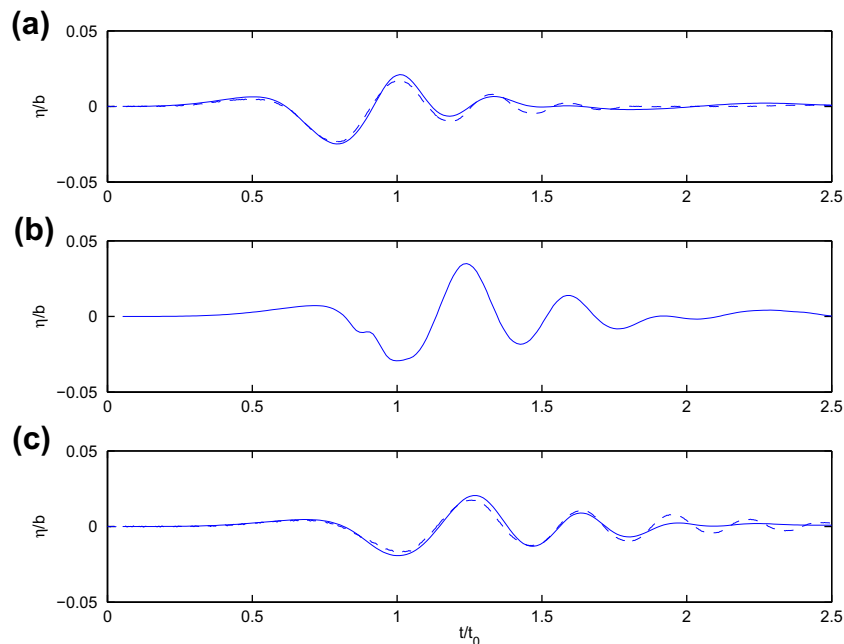


Fig. 16. Comparisons between numerical nonhydrostatic results (solid lines) and experimental data (dashed lines) for free surface elevation for landslide-generated waves at three wave gauges with initial depth of submergence $d = 120$ mm. Gauge coordinates (x, y) : (a) (1469, 350) mm; (b) (1929, 0) mm; (c) (1929, 500) mm. Experimental data are not available for (b).

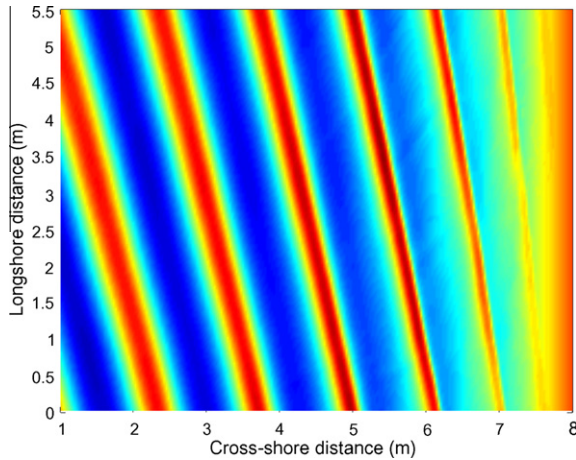


Fig. 17. A snapshot of computed surface elevation of case 4 in Visser's experiment (1991).

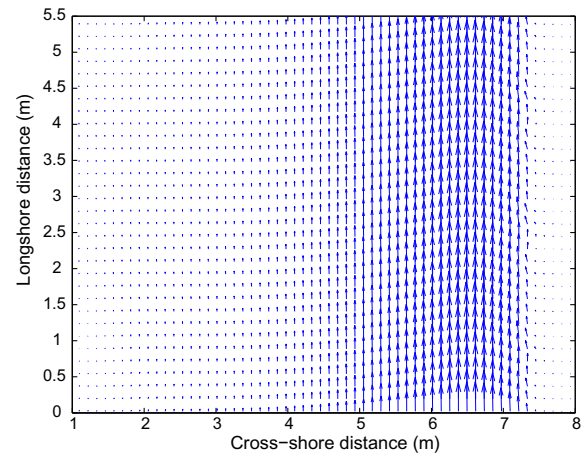


Fig. 18. Phase-averaged current field (averaged by 5 waves) of case 4 in Visser's experiment (1991).

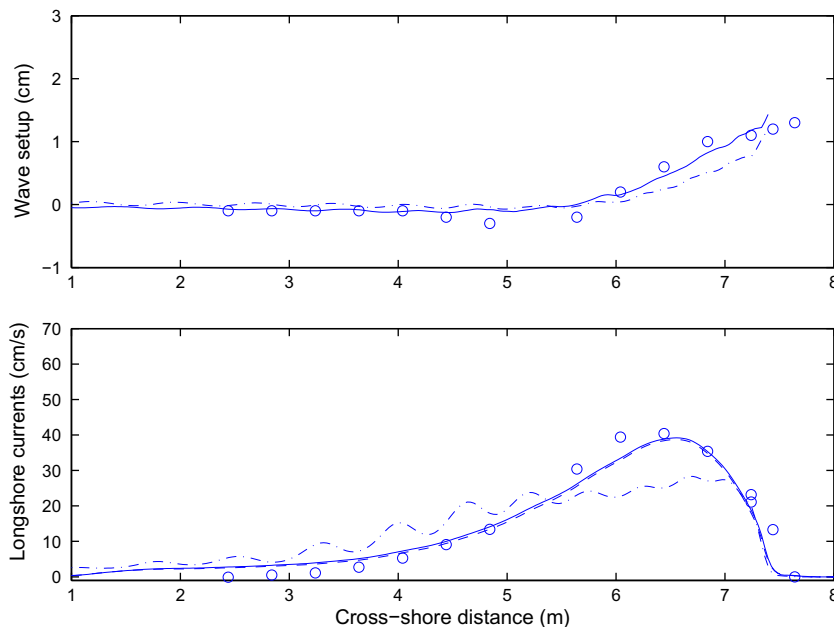


Fig. 19. Comparisons of computed wave setup (upper panel) and longshore currents (lower panel) at $t = 110$ s with experimental data (Visser, 1991). The dashed line shows the computed phase-averaged longshore current at 100 s. The dash-dotted line shows the computed wave setup and longshore currents without turbulent diffusion at $t = 110$ s.

Meanwhile, the longshore current is largely underestimated and not as smooth as that with turbulent diffusion. These results further prove that turbulent diffusion has little impact on free surface predictions in the surf zone, but has significant effects on wave-induced currents as found by Bradford (2011).

5. Conclusions

In this paper, NHWAVE, a shock-capturing non-hydrostatic model for nonlinear free-surface wave processes is presented. The governing equations are solved in a σ coordinate system and discretized by a combined finite volume and finite difference scheme with a Godunov-type method. In order to apply Godunov-type scheme, the velocities are collocated at the cell center. The dynamic pressure is defined at the vertical cell faces, which ensure that the pressure boundary condition at the free surface can be precisely prescribed. The HLL approximate Riemann solver was employed to estimate fluxes at horizontal cell faces. The sec-

ond-order nonlinear Strong Stability-Preserving (SSP) Runge–Kutta scheme were adopted for adaptive time stepping.

The model was tested using seven benchmarks based on analytical solutions or experimental data. Unlike some other non-hydrostatic models which need 10–20 vertical layers to well simulate short waves, the present model can achieve good predictions of wave shoaling, wave dispersion, refraction and diffraction using 3–5 vertical layers. With the Godunov-type scheme, which is suitable for solving discontinuous solutions, the model can be used to study complex problems such as wave breaking in the surf zone. For the landslide generated tsunami, the model predicts the evolution of surface elevation generally well.

Acknowledgements

The authors thank two anonymous reviewers whose detailed comments greatly improved the quality of this manuscript. This work was supported by the Office of Naval Research (Coastal Geo-

sciences Program), the National Science Foundation (Physical Oceanography) and the Delaware Sea Grant College Program.

References

- Agnon, Y., Madsen, P.A., Schäffer, H.A., 1999. A new approach to high order Boussinesq models. *J. Fluid Mech.* 399, 319–333.
- Ai, C., Jin, S., 2010. Non-hydrostatic finite volume method for non-linear waves interacting with structures. *Comput. Fluids* 39, 2090–2100.
- Beji, S., Battjes, J.A., 1993. Experimental investigation of wave propagation over a bar. *Coastal Eng.* 19, 151–162.
- Berkhoff, J.C.W., Booy, N., Radder, A.C., 1982. Verification of numerical wave propagation models for simple harmonic linear water waves. *Coastal Eng.* 6, 255–279.
- Bradford, S.F., 2005. Godunov-based model for nonhydrostatic wave dynamics. *J. Waterway Port Coastal Ocean Eng.* 131, 226–238.
- Bradford, S.F., 2011. Nonhydrostatic model for surf zone simulation. *J. Waterway Port Coastal Ocean Eng.* 137 (4), 163–174.
- Casulli, V., Stelling, G.S., 1998. Numerical simulation of 3D quasi-hydrostatic free-surface flows. *J. Hydrol. Eng.* 124, 678–686.
- Casulli, V., 1999. A semi-implicit finite difference method for non-hydrostatic, free-surface flow. *Int. J. Numer. Methods Fluids* 30, 425–440.
- Casulli, V., Zanolli, P., 2002. Semi-implicit numerical modeling of nonhydrostatic free-surface flows for environmental problems. *Math. Comput. Model.* 36, 1131–1149.
- Chen, Q., Madsen, P.A., Basco, D.R., 1999. Current effects on nonlinear interactions of shallow-water waves. *J. Waterway Port Coastal Ocean Eng.* 125 (4), 176–186.
- Chen, Q., Kirby, J.T., Dalrymple, R.A., Shi, F., Thornton, E.B., 2003. Boussinesq modeling of longshore currents. *J. Geophys. Res.* 108. doi:10.1029/2002JC001308.
- Chen, X., 2003. A fully hydrodynamic model for three-dimensional, free-surface flows. *Int. J. Numer. Methods Fluids* 42, 929–952.
- Christensen, E.D., 2006. Large eddy simulation of spilling and plunging breakers. *Coastal Eng.* 53, 463–485.
- Enet, F., Grilli, S.T., 2007. Experimental study of tsunami generation by three-dimensional rigid underwater landslides. *J. Waterway Port Coastal Ocean Eng.* 133, 442–454.
- Fringer, O.B., Gerritsen, M., Street, R.L., 2006. An unstructured-grid, finite-volume, nonhydrostatic, parallel coastal ocean simulator. *Ocean Modell.* 14, 139–173.
- Fuhrman, D.R., Madsen, P.A., 2009. Tsunami generation, propagation and run-up with a high-order Boussinesq model. *Coastal Eng.* 56, 747–758.
- Gobbi, M.F., Kirby, J.T., 1999. Wave evolution over submerged sills: tests of a high-order Boussinesq model. *Coastal Eng.* 37, 57–96.
- Gobbi, M.F., Kirby, J.T., Wei, G., 2000. A fully nonlinear Boussinesq model for surface waves. II. Extension to $O(kh^4)$. *J. Fluid Mech.* 405, 181–210.
- Gottlieb, S., Shu, C.-W., Tadmor, E., 2001. Strong stability-preserving high-order time discretization methods. *SIAM Rev.* 43, 89–112.
- Harlow, F.H., Welch, J.E., 1965. Numerical calculation of time-dependent viscous incompressible flow of fluid with free surface. *Phys. Fluids* 8, 2182–2189.
- Harten, A., Lax, P., van Leer, B., 1983. On upstream differencing and Godunov-type schemes for hyperbolic conservation laws. *SIAM Rev.* 25, 35.
- Hirt, C.W., Nichols, B.D., 1981. Volume of fluid (VOF) method for the dynamics of free boundaries. *J. Comput. Phys.* 39, 201–225.
- Kim, D.H., Cho, Y.-S., Kim, H.J., 2008. Well-balanced scheme between flux and source terms for computation of shallow-water equations over irregular bathymetry. *J. Eng. Mech.* 134, 277–290.
- Kim, D.H., Lynett, P.J., Socolofsky, S.A., 2009. A depth-integrated model for weakly dispersive, turbulent, and rotational fluid flows. *Ocean Modell.* 27, 198–214.
- Kim, D.H., Lynett, P.J., 2011. Turbulent mixing and scalar transport in shallow and wavy flows. *Phys. Fluids* 23, 016603.
- Lai, Z., Chen, C., Cowles, G.W., Beardsley, R.C., 2010. A nonhydrostatic version of FVCOM: 1. Validation experiments. *J. Geophys. Res.* 115. doi:10.1029/2009JC005525.
- Larsen, J., Dancy, H., 1983. Open boundaries in short-wave simulations – a new approach. *Coastal Eng.* 7 (3), 285–297.
- Lee, J.W., Terbner, M.D., Nixon, J.B., Gill, P.M., 2006. A 3-D non-hydrostatic pressure model for small amplitude free surface flows. *Int. J. Numer. Methods Fluids* 50, 649–672.
- Li, B., Fleming, C., 2001. Three-dimensional model of Navier–Stokes equations for water waves. *J. Waterway Port Coastal Ocean Eng.*, 16–25.
- Liang, Q., Marche, F., 2009. Numerical resolution of well-balanced shallow water equations with complex source terms. *Adv. Water Resour.* 32, 873–884.
- Lin, P., Li, C.W., 2002. A σ -coordinate three-dimensional numerical model for free surface wave propagation. *Int. J. Numer. Methods Fluids* 38, 1045–1068.
- Lin, P., Liu, P.L.-F., 1998a. A numerical study of breaking waves in the surf zone. *J. Fluid Mech.* 359, 239–264.
- Lin, P., Liu, P.L.-F., 1998b. Turbulent transport, vorticity dynamics, and solute mixing under plunging breaking waves in surf zone. *J. Geophys. Res.* 103, 15677–15694.
- Lynett, P., Liu, P.L.-F., 2002. A two-layer approach to wave modelling. *Proc. Roy. Soc. A* 460, 2637–2669.
- Ma, G., Shi, F., Kirby, J.T., 2011. A polydisperse two-fluid model for surf zone bubble simulation. *J. Geophys. Res.* 116. doi:10.1029/2010JC006667.
- Madsen, P.A., Sørensen, O.R., 1992. A new form of the Boussinesq equations with improved linear dispersion characteristics. Part A slowly-varying bathymetry. *Coastal Eng.* 18, 183–204.
- Namin, M., Lin, B., Falconer, R., 2001. An implicit numerical algorithm for solving non-hydrostatic free-surface flow problems. *Int. J. Numer. Methods Fluids* 35, 341–356.
- Nwogu, O., 1993. Alternative form of Boussinesq equations for nearshore wave propagation. *J. Waterway Port Coastal Ocean Eng.* 119, 618–638.
- Osher, A., Sethian, J.A., 1988. Fronts propagating with curvature-dependent speed: algorithms based on Hamilton–Jacobi formulations. *J. Comput. Phys.* 79, 12–49.
- Patankar, S.V., 1980. *Numerical Heat Transfer and Fluid Flow*. McGraw-Hill, New York.
- Phillips, N.A., 1957. A coordinate system having some special advantages for numerical forecasting. *J. Meteor.* 14, 184–185.
- Shi, F., Kirby, J.T., Ma, G., 2010. Modeling quiescent phase transport of air bubbles induced by breaking waves. *Ocean Modell.* 35, 105–117.
- Stelling, G., Zijlema, M., 2003. An accurate and efficient finite-difference algorithm for non-hydrostatic free-surface flow with application to wave propagation. *Int. J. Numer. Methods Fluids* 43, 1–23.
- Synolakis, C.E., 1987. The runup of solitary waves. *J. Fluid Mech.* 185, 523–545.
- Tanaka, M., 1986. The stability of solitary waves. *Phys. Fluids* 29, 650–655.
- Visser, P.J., 1991. Laboratory measurements of uniform longshore currents. *Coastal Eng.* 15, 563–593.
- Watanabe, Y., Saeki, H., Hosking, R.J., 2005. Three-dimensional vortex structures under breaking waves. *J. Fluid Mech.* 545, 291–328.
- Walters, R.A., 2005. A semi-implicit finite element model for non-hydrostatic (dispersive) surface waves. *Int. J. Numer. Methods Fluids* 49, 721–737.
- Wei, G., Kirby, J.T., Grilli, S.T., Subramanya, R., 1995. A fully nonlinear Boussinesq model for surface waves. Part 1. Highly nonlinear unsteady waves. *J. Fluid Mech.* 294, 71–92.
- Wu, C.H., Young, C.-C., Chen, Q., Lynett, P.J., 2010. Efficient nonhydrostatic modeling of surface waves from deep to shallow water. *J. Waterway Port Coastal Ocean Eng.* 136, 104–118.
- Young, C.-C., Wu, C.-H., Kuo, J.-T., Liu, W.-C., 2007. A higher-order σ -coordinate non-hydrostatic model for nonlinear surface waves. *Ocean Eng.* 34, 1357–1370.
- Young, C.-C., Wu, C.-H., Liu, W.-C., Kuo, J.-T., 2009. A higher-order non-hydrostatic σ model for simulating nonlinear refraction–diffraction of water waves. *Coastal Eng.* 56, 919–930.
- Young, C.-C., Wu, C.-H., 2010. A σ -coordinate non-hydrostatic model with embedded Boussinesq-type-like equations for modeling deep-water waves. *Int. J. Numer. Methods Fluids* 63, 1448–1470.
- Yuan, H., Wu, C.-H., 2004a. A two-dimensional vertical non-hydrostatic σ model with an implicit method for free-surface flows. *Int. J. Numer. Methods Fluids* 44, 811–835.
- Yuan, H., Wu, C.-H., 2004b. An implicit three-dimensional fully non-hydrostatic model for free-surface flows. *Int. J. Numer. Methods Fluids* 46, 709–733.
- Zhou, J.G., Gauson, D.M., Mingham, C.G., Ingram, D.M., 2001. The surface gradient method for the treatment of source terms in the shallow-water equations. *J. Comput. Phys.* 168, 1–25.
- Zijlema, M., Stelling, G.S., 2005. Further experiences with computing non-hydrostatic free-surface flows involving water waves. *Int. J. Numer. Methods Fluids* 48, 169–197.
- Zijlema, M., Stelling, G.S., 2008. Efficient computation of surf zone waves using the nonlinear shallow water equations with non-hydrostatic pressure. *Coastal Eng.* 55, 780–790.